

## Efficient bifacial DSSCs through disorder by design

José M. Miranda-Muñoz, Sol Carretero-Palacios, Alberto Jiménez-Solano, Yuelong Li, Gabriel Lozano and Hernán Míguez.

SUPPLEMENTARY INFORMATION

## Efficient bifacial DSSCs through disorder by design

### SUPPLEMENTARY INFORMATION

José M. Miranda-Muñoz, Sol Carretero-Palacios, Alberto Jiménez-Solano, Yuelong Li, Gabriel Lozano and Hernán Míguez.

- Experimental spectral refractive index and extinction coefficient used in the simulations:

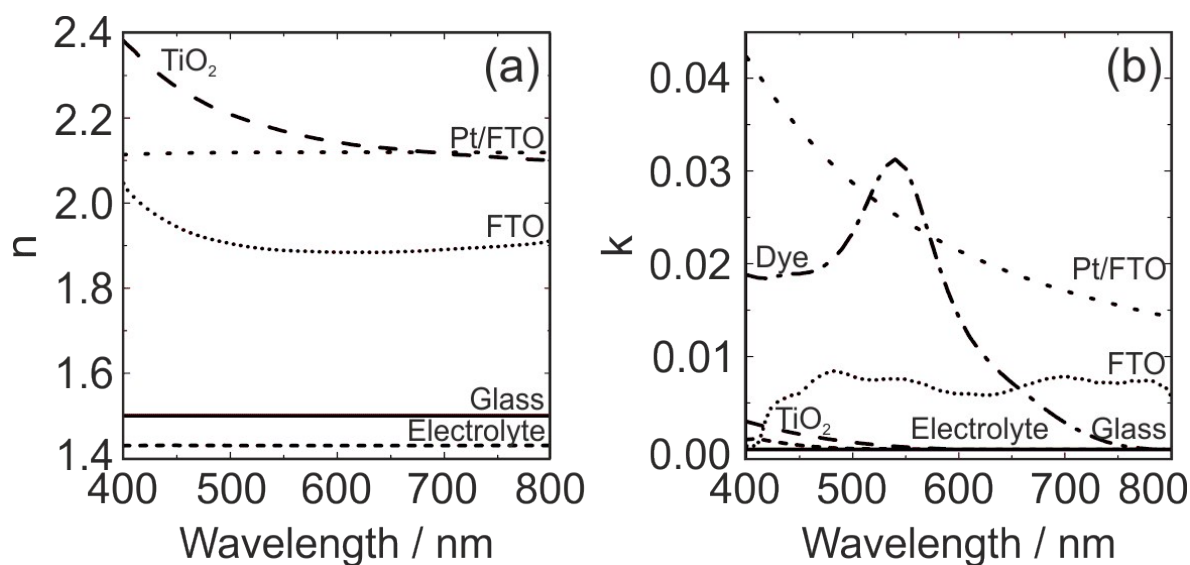


Figure S1. Spectral dependence of the complex refractive index of each material comprising the solar cell. (a) Real part of the refractive index. b) Imaginary part of the refractive index.

- Optical properties of the Pt-coated FTO glass system employed as counterelectrode:

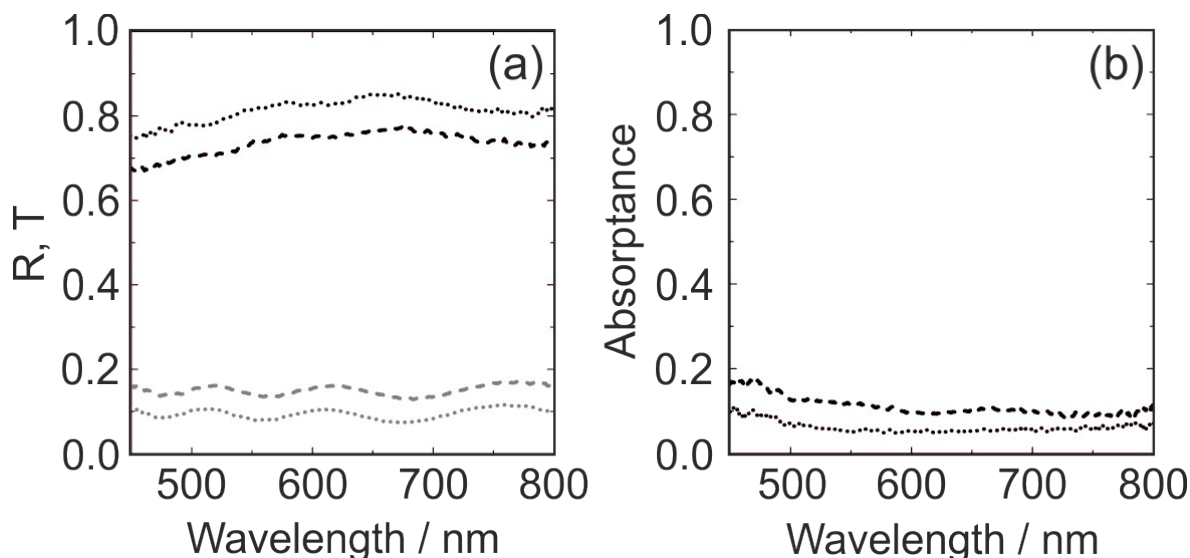


Figure S2. Optical properties of the Pt counterelectrodes. (a) Reflectance (grey lines) and transmittance (black lines) curves. (b) Absorbance curves. The dashed lines correspond to the Pt-coated counter electrode, whereas data for a bare FTO glass has also been included for comparison (dotted lines). The measurements were performed for light impinging on the Pt side in the case of the counter electrodes and on the FTO side for the bare reference FTO glass substrate.

The conditions for the coating of the FTO-glass substrates employed as counterelectrodes were studied in order to concomitantly optimize their transparency and maximize operation of the cells. Two parameters, the concentration of the chloroplatinic acid hexahydrate (in 2-propanol) solution and the number of depositions by spin-coating technique, were tested to that aim. In particular, the best results were observed for counterelectrodes prepared by performing 3 coatings by spin coating, with a subsequent drying process at 80°C during 5 minutes between coatings, employing a 0.6mM chloroplatinic acid hexahydrate (in 2-propanol) solution. The optical properties for such counterelectrodes are displayed in Fig.S2. The left panel, Fig.S2(a), shows that transmittance of the Pt-coated FTO-glass substrate is mostly above 70% throughout the visible part of the spectrum where the dye molecules absorb, specially in the red range, where absorbance enhancement is aimed at. The reflectance and transmittance curves corresponding to a bare FTO-glass substrate have been included for comparison. At the same time, no big increase is observed regarding absorbance, Fig.S2(b), with respect to the bare FTO-glass. The absorbance values for the Pt-coated counterelectrode are maintained below 15% in most of the measured range, reaching 10% from 600 nm onwards.

- Comparison of the scattering efficiencies of a sphere and a cube embedded in the system:

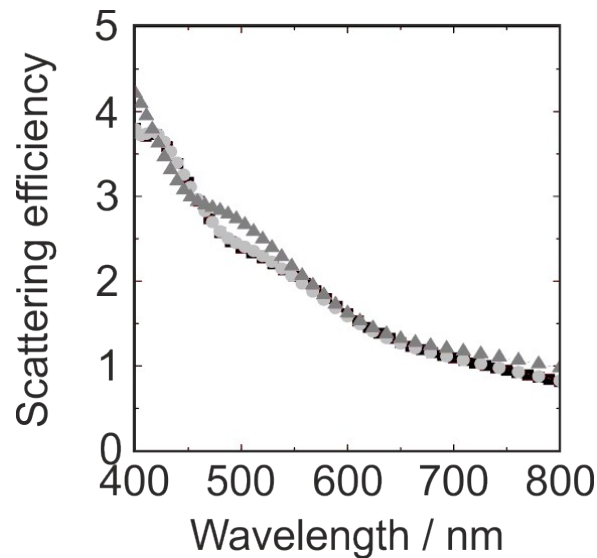


Figure S3. Simulated scattering efficiency of a  $\text{TiO}_2$  sphere of radius  $r = 150$  nm (light grey circles) and a cube of the same volume (dark grey triangles) using 3-dimensional Finite-difference time-domain numerical analysis (FDTD) employing the software “FDTD Solutions” from Lumerical Solutions. For comparison, the analytical calculation employing scattering Mie theory for spheres is also shown (black squares). A shell with the same geometry as the nanoparticle filled with electrolyte is considered in all cases, with the same volume as that of a spherical shell of  $sh = 0.5 \cdot r$  correspondingly.

- Discussion about the presence of a shell surrounding the  $\text{TiO}_2$  scattering centers:

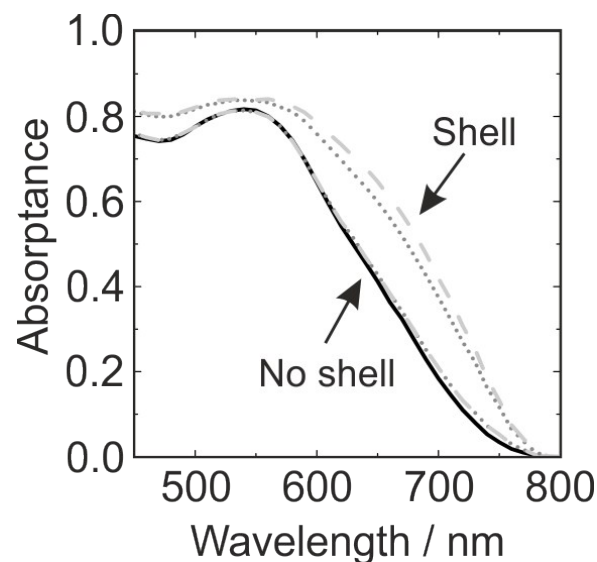


Figure S4. Simulated absorbance curves in the sensitized layer of a complete solar cell under front illumination with an electrode including scatterer centers with and without shell (as indicated). Solid black line: reference; short-dotted grey line: 5% filling fraction; dashed grey line: 7.5% filling fraction. Scatterer radius:  $r = 85$  nm; shell thickness:  $sh = 0.5 \cdot r$ .

Scanning Electron Microscopy images of the nanocrystalline scattering centers embedded in the mesoporous  $\text{TiO}_2$  matrix revealed the presence of a hollow shell around those, probably due to shrinking effects during crystallization. The need to include an element in the model accounting for this arose when calculating the absorptance curves in the sensitized layer of a complete cell, Fig. S1, where these curves are plotted for cells containing  $\text{TiO}_2$  inclusions with 5% and 7.5% filling fraction, along with that for a reference cell (black solid line). If the shell, filled with electrolyte, is not considered, not only the improvement with respect to the reference is hardly noticeable, but the curves for the cells with inclusions look virtually identical, revealing no enhancement when increasing the filling fraction value. This behaviour, inconsistent with the experiments, is overcome if an electrolyte-filled shell surrounding the scatterers is taken into account. In this case, not only is a clear improvement evident, but also is an enhancement dependent on the filling fraction percentage consistently reproduced. Several tests revealed that experiments were best reproduced if the shell height,  $sh$ , was considered to be  $sh = 0.5 \cdot r$ , i.e., half the radius of the scatterer.

- Upper limit short-circuit current density maps for isotropic angular distribution of the scattered light:

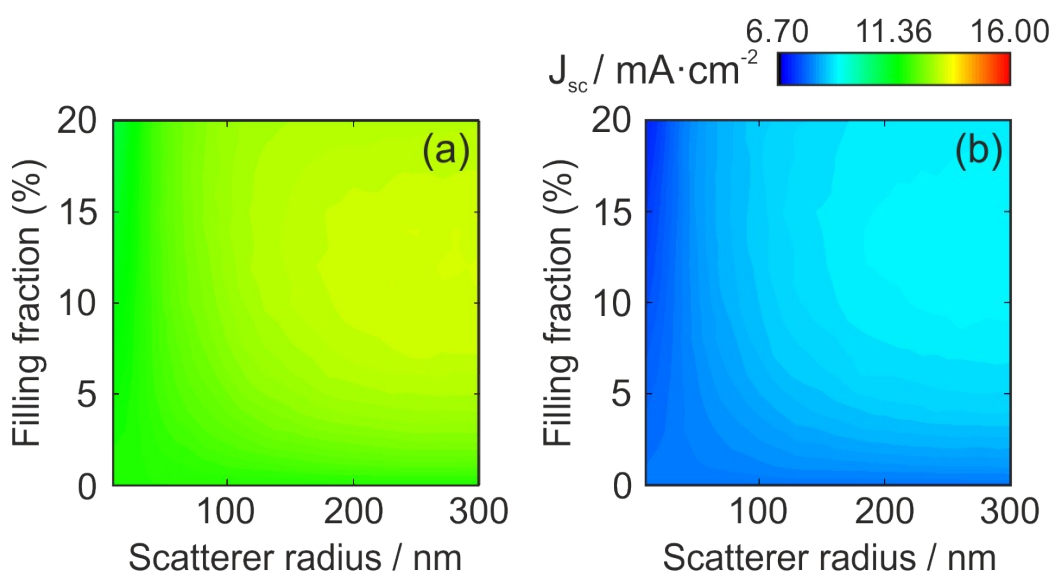


Figure S5. Upper limit for the short-circuit current density of a simulated device under (a) front and (b) rear illumination in relation to the filling fraction percentage and the radius value of the scattering centers considering the hypothetical situation of having an isotropic angular distribution of the scattered light and the same scattering intensity than in the case of the sphere surrounded by a shell.

In order to assess the influence of the angular distribution of the scattering in the performance of the cell, further simulations were performed. The upper limit  $J_{sc}$  values as a function of the filling fraction and radius of the nanocrystalline  $\text{TiO}_2$  spheres are displayed in Fig. S4 for a situation in which hypothetical scattering centers featuring equal scattered light probability for all the angles and the same scattering intensity than in the case of a sphere surrounded by a shell is considered. The advantageous effect of inducing a narrow-forward angular distribution of the scattered light inside the photoanode, associated to the spherical inclusions addressed in Fig. 1(c) in the main manuscript, is reinforced after exploring the nonfactual situation in which wholly isotropic scattering is considered. When comparing to the colour maps in Fig.1 in the main manuscript, lower values for the upper limit  $J_{sc}$  are attainable for the whole parameter range considered in the maps, being the maximum  $J_{sc} = 13.2 \text{ mA} \cdot \text{cm}^{-2}$ , which corresponds to around 13% enhancement, in both front and rear operation, with respect to a reference cell, in contrast to the maximum 35%  $J_{sc}$  enhancement expected when including spherical nanocrystalline  $\text{TiO}_2$  scattering centers yielding a narrow-forward angular distribution of the scattered light. The reason for such decrease lies in the equal probability of having backward and forward scattering, instead of being this restricted to a narrow forward angular region. If backward scattering is as probable as forward, optical losses through reflection become significant, resulting in a shorter amount of the incident light used for absorption.

- SEM images:

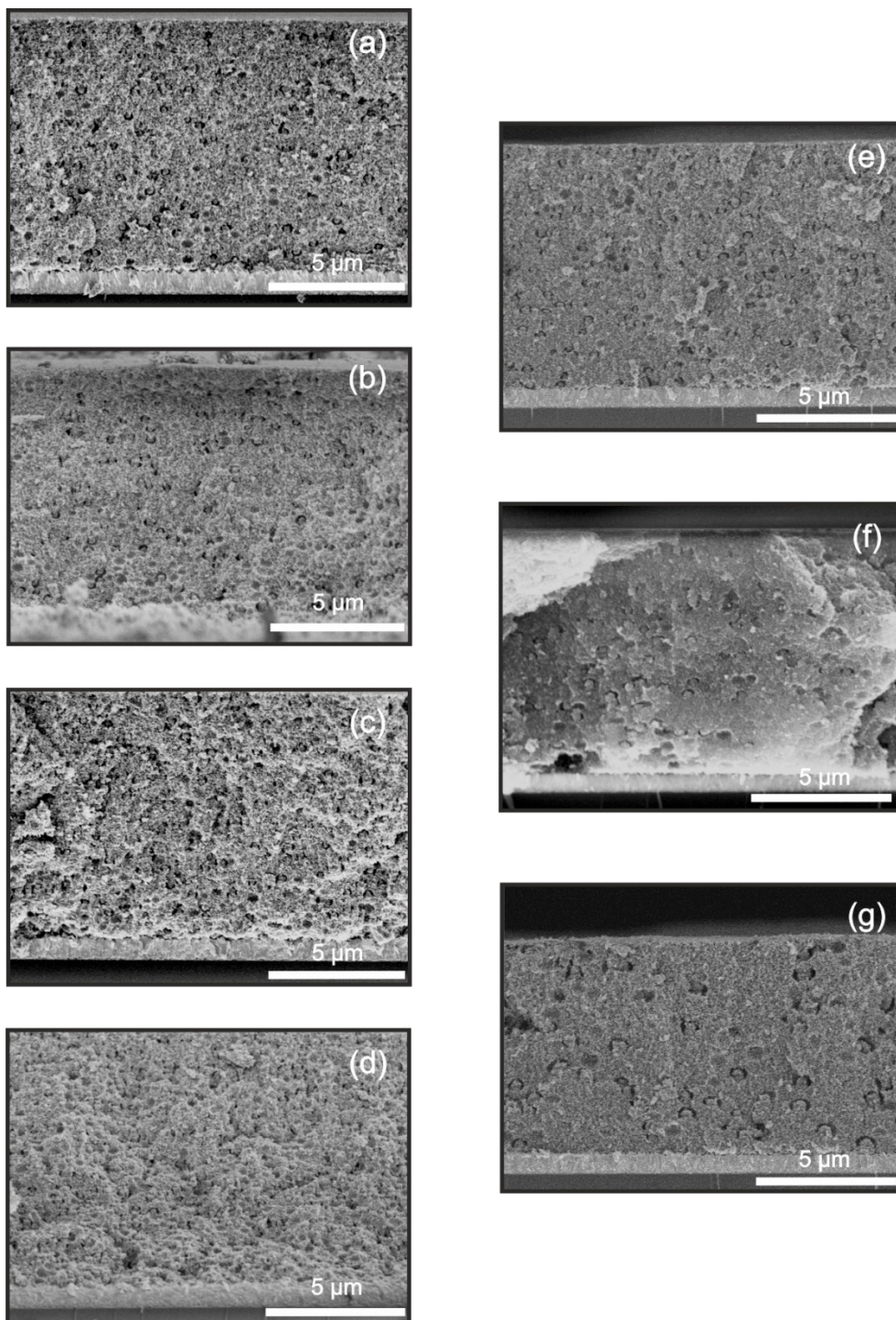


Figure S6. Scanning Electron Microscopy images of 8- $\mu\text{m}$  thick porous  $\text{TiO}_2$  electrodes embedding  $\text{TiO}_2$  nanospheres for different filling fraction percentages and scatterer sizes. (a) 5% filling fraction and  $100 \pm 15$  nm scatterer radius. (b) 7.5% filling fraction and  $100 \pm 15$  nm scatterer radius. (c) 10% filling fraction and  $100 \pm 15$  nm scatterer radius. (d) 20% filling fraction and  $100 \pm 15$  nm scatterer radius. (e)  $100 \pm 15$  nm scatterer radius and 10% filling factor. (f)  $135 \pm 15$  nm scatterer radius and 10% filling factor. (g)  $200 \pm 25$  nm scatterer radius and 10% filling factor.

- Discussion about the independence of the absorptance enhancement on the illumination side:

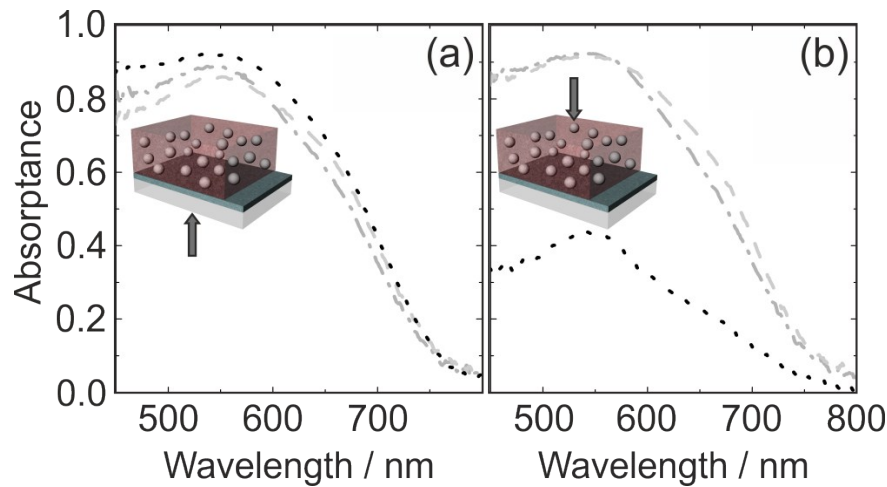


Figure S7. Experimental absorptance curves by the dye in the described system under (a) front and (b) rear illumination for two samples containing different filling fraction values: 10% (dot-dashed grey line) and 20% (dashed grey line), and the same scatterer radius ( $100 \pm 15$  nm). The absorptance curve corresponding to a bare system with a scattering overlayer on top of the sensitized film has been included (dotted black line) in order to remark the dependence of the efficacy of the approach on the illumination side.

The behaviour of the absorptance when illuminating from both sides was tested. This was performed for two samples with different filling fractions and the same scatterer size. We observed how the enhancement in the absorptance is mostly independent on the illumination side. This is due to the disordered nature of the approach. The random distribution of the scatterers in the electrode results in an absence of symmetry, existing therefore no preferential side for illumination so as to induce a more beneficial scattering effect. The light is scattered in the same way when illuminating from any of both sides and the absorptance enhancement displays very similar behaviour. In contrast, the illumination side is crucial when including a back scattering layer, as absorptance enhancement is only observed under front illumination. Rear illumination yields a major decrease.

- Discussion about the haze and its influence on light scattering efficiency:

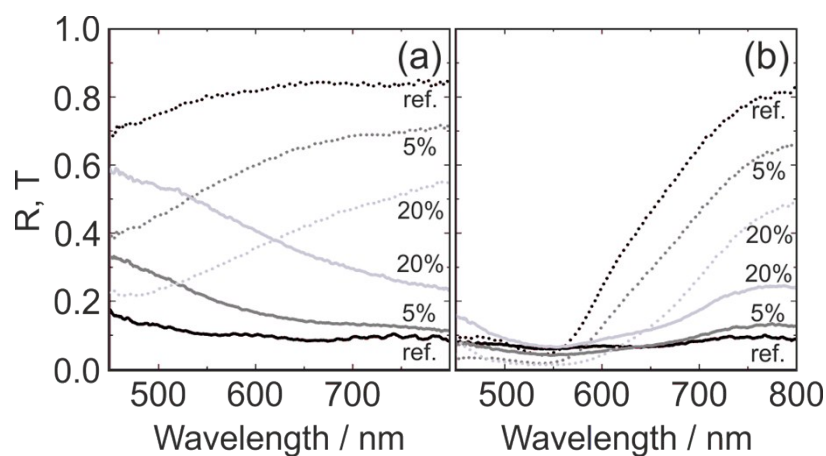


Figure S8. Experimental total reflectance (solid lines) and transmittance (dotted lines) curves for the rear-illuminated system described in the main manuscript for the analysis of Fig. 3 for 5% and 20% filling fraction and a reference system for comparison. The curves were obtained (a) before and (b) after dye soaking. Black lines: references; grey lines: systems including scattering particles. Scatterer radius:  $100 \pm 15$  nm.

Measurement of diffuse reflectances and transmittances are usually considered a way to evaluate the ability of the system at scattering and trapping light inside. There is, in fact, a spectral magnitude, the haze, that accounts for the amount of scattered light by a material and it is defined as the ratio of the diffused transmittance to the total transmittance. High values of the haze have been claimed to be required in order to obtain high  $\eta_{IPCE}$  in the red region, due to the small extinction coefficient of the dye in this region of the visible spectrum.<sup>40</sup> This can, nevertheless, be misleading when aiming at characterizing light trapping. An electrode containing scattering centers localized along the first few microns inside the active layer would also render high diffuse reflectances and transmittances, yet most of the light escapes the system by reflection as optical losses while its path length is not being relevantly enlarged inside. No significant information is therefore provided by the diffuse magnitudes when aiming at light scattering for efficient increase of the residence time of the photons inside the system. During this study, complete optical characterization of the films was performed. Total reflectance and transmittance for a couple of filling fraction percentages are shown in Fig. S6. The increase in the reflectance observed in Fig. S6(a) for higher filling fraction values is exclusively due to the diffuse reflectance (confirmed through measurement of the diffuse magnitudes). Nonetheless, when observing the reflectance curves in Fig. S6(b), it is visible that very little losses due to reflection are present in the region where the dye absorbs most efficiently, regardless the scatterer loading in the film. An analogue observation is possible for the transmittances. This observation points out the ability of our system at increasing the path length of photons inside the electrode due to the random distribution of the nanocrystalline scatterers. High diffuse reflectance and transmittance is not translated in this case into losses, since similar transmittances and reflectances are measured in a specific wavelength range in the sensitized film, no matter whether the electrode presents inclusions or not.

- Influence of the scatterer size in the performance of the device:

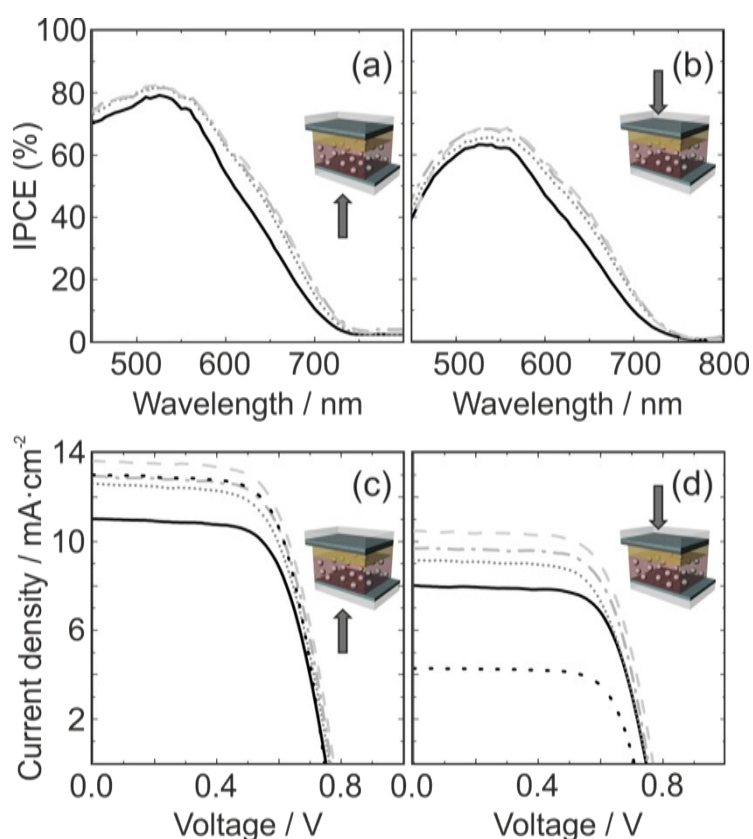


Figure S9. Experimental incident photon to current efficiency and Current density-Voltage curves for complete cells with different scatterer radius values and 10% filling fraction. (a) Experimental  $\eta_{IPCE}$  curves for front illumination. (b) Experimental  $\eta_{IPCE}$  curves for rear illumination. (c)  $J$ - $V$  characteristics for front illumination. (d)  $J$ - $V$  characteristics for rear illumination. Solid black line: reference, short-dotted grey line:  $r = 100 \pm 15$  nm, dash-dotted grey line:  $r = 135 \pm 15$  nm, dashed grey line:  $r = 200 \pm 25$  nm, dotted black line: cell with a back scattering layer. Electrode thickness: 8  $\mu\text{m}$ .

Experiments were performed in order to study the influence of the scatterer size in the performance of the device. In this case, the filling fraction was fixed to 10% and three different scatterer radii were tested, namely,  $100 \pm 10$  nm,  $135 \pm 15$  nm,  $200 \pm 25$  nm. The same trends to those obtained for the experiments in the main manuscript, in which the filling fraction was varied, are visible here again.

- Calculated incident photon to current efficiency curves:

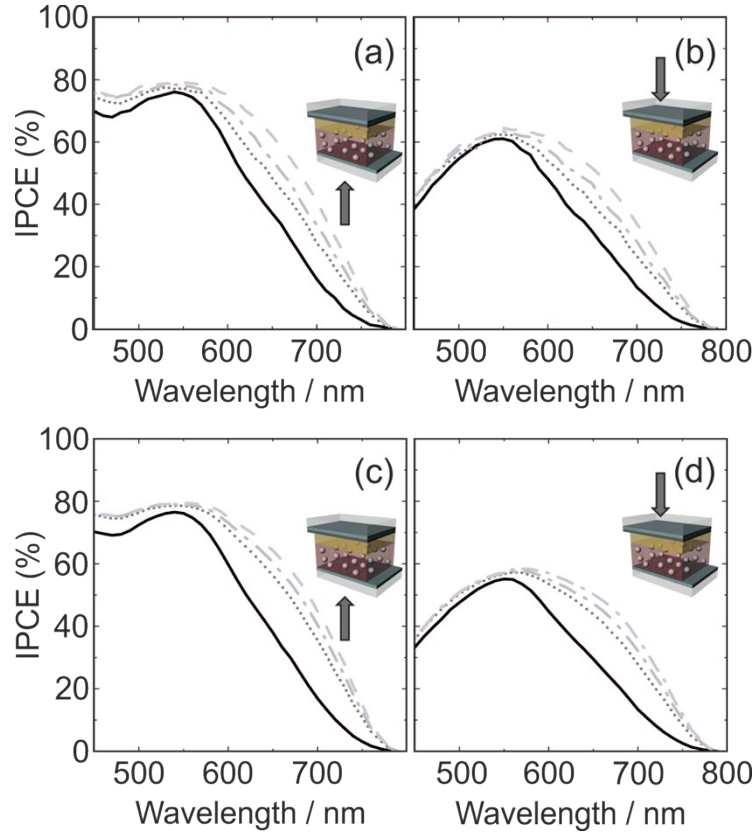


Figure S10. Theoretical incident photon to current efficiency for complete cells with different (a), (b) filling fractions and (c), (d) scatterer radius values. (a), (b) scatterer radius: 160 nm. Solid black line: reference, short-dotted grey line: ff = 5%, dash-dotted grey line: ff = 10%, dashed grey line: ff = 15%, dotted black line: cell with a back scattering layer. (a) Experimental  $\eta_{IPCE}$  curves for front illumination. (b) Experimental  $\eta_{IPCE}$  curves for rear illumination. (c)  $J$ - $V$  characteristics for front illumination, (d)  $J$ - $V$  characteristics for rear illumination. Solid black line: reference, short-dotted grey line:  $r = 100 \pm 15$  nm, dash-dotted grey line:  $r = 135 \pm 15$  nm, dashed grey line:  $r = 200 \pm 25$  nm, dotted black line: cell with a back scattering layer. Electrode thickness:  $8 \mu\text{m}$ .

It is assumed that  $\eta_{inj}(\lambda) = \eta_{reg}(\lambda) = 1$ , and thus  $\eta_{IPCE}(\lambda) = \eta_{LHE}(\lambda)\eta_{col}(\lambda)$ . Collection efficiency is computed from the electron generation function  $g(\lambda, x)$ , with  $x$  defined along incident light propagation, like:

$$\eta_{col}(\lambda) = \frac{\int_0^d g(\lambda, x) \cdot \frac{\cosh\left(\frac{d-x}{L_e}\right)}{\cosh\left(\frac{d}{L_e}\right)} dx}{\int_0^d g(\lambda, x) dx}$$

Being  $L_e$  a fitting parameter accounting for the 'effective' electron diffusion length, i.e., the average distance covered by the electron before recombination, and  $d$  the electrode thickness. Best fitting is obtained for  $L_e = 18$   $\mu\text{m}$ .

- Estimation of the electron collection efficiency of the devices:

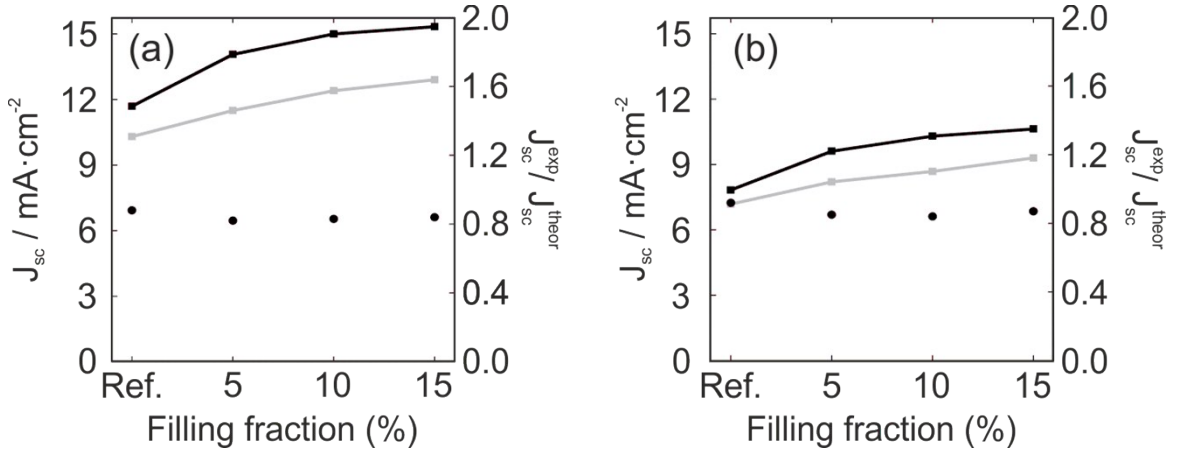


Figure S11. Theoretical upper short circuit current density values (black connected squares) and experimental short circuit current density values (grey connected squares) of the devices with particle radius fixed to  $160 \pm 50$  nm and variable filling fraction percentage under (a) front and (b) rear illumination. Values of the  $J_{sc}$  discrepancy from the experimental values to the upper limit are plotted as well in black dots.

An estimation of the collection efficiency of the devices studied in the main manuscript can be done through comparison of the experimental  $J_{sc}$  values with the upper limit calculated via modelling.  $J_{sc}$  is calculated according to:

$$J_{sc} = q \int_{\lambda_1}^{\lambda_2} d\lambda \eta_{IPCE}(\lambda) \Phi(\lambda)$$

where  $q$  is the electron charge,  $\Phi(\lambda)$  the spectral incident photon flux, corresponding to the AM1.5 Solar Emission Spectrum under our circumstances, and  $\eta_{IPCE}(\lambda)$  the wavelength-dependent incident photon to current efficiency, also referred to as external quantum efficiency (EQE):

$$\eta_{IPCE}(\lambda) = \eta_{LHE}(\lambda) \eta_{col}(\lambda) \eta_{inj}(\lambda) \eta_{reg}(\lambda),$$

a product of efficiencies. Here,  $\eta_{LHE}(\lambda)$  refers to the light harvesting absorption efficiency, namely, the absorbance by the dye in the active layer,  $\eta_{col}(\lambda)$ , represents the charge-collection efficiency,  $\eta_{inj}(\lambda)$  is the electron injection efficiency from the dye into the titania matrix and  $\eta_{reg}(\lambda)$  alludes to the effectiveness in the process of regeneration of the dye. The values of  $\eta_{inj}(\lambda)$  and  $\eta_{reg}(\lambda)$  are typically assumed 1. For the generation of the maps in Fig. 1(e) and (f) in the main manuscript,  $\eta_{col}(\lambda)$  was also assumed 1, so that the value of  $J_{sc}$  is exclusively dependent on the absorption in the electrode and expresses an upper limit for the experimental performance of the cells in the ideal situation where each generated electron contributes to the photocurrent.

Assuming that both, injection and dye regeneration efficiency, are still experimentally close to 1, we can state that decrease in the  $J_{sc}$  values with respect to the upper theoretical limit is exclusively due to the collection efficiency. From the  $J_{sc}$  correction values in Fig. S9, we can estimate an electron collection efficiency around 0.9. Such estimation is legitimate after the previous verification that the absorbance calculations duly predict the experimental results (Fig. 3 in the main manuscript).